

Phosphorus Chemistry in the Earth’s Upper Atmosphere

John M.C. Plane^{1*}, Wuhu Feng^{1,2} and Kevin M. Douglas¹

¹ School of Chemistry, University of Leeds, UK

² National Centre for Atmospheric Science and School of Earth and Environment, University of Leeds, UK

Corresponding author: John Plane (j.m.c.plane@leeds.ac.uk)

Submitted July 2021.

Keywords: phosphorus; interplanetary dust; meteoric ablation; mesospheric chemistry; meteoric smoke; pre-biotic chemistry

Key points:

- a reaction network is developed in a global model for exploring the chemistry of meteor-ablated phosphorus in the earth’s upper atmosphere
- a narrow layer of OPO is predicted to occur globally around 90 km, analogous to the layers of meteor-ablated Na and Fe
- a significant flux of bio-available metal phosphites is predicted to be deposited at the Earth’s surface

Abstract.

The ablation of phosphorus from interplanetary dust particles entering the Earth’s atmosphere is a potentially significant source of this key bio-element. In this study, the atmospheric chemistry of phosphorus is explored by developing a reaction network of possible routes from PO, the major ablation product in the upper mesosphere/lower thermosphere region, to the stable reservoirs H_3PO_3 and H_3PO_4 that become incorporated into meteoric smoke particles as metal phosphites and phosphates, respectively. The network is constructed with reactions whose kinetics have been measured experimentally, together with reactions where theoretical rate coefficients are estimated using a combination of electronic structure theory calculations and a Rice-Ramsperger-Kassel-Markus master equation treatment. The network is then incorporated into a global chemistry-climate model, together with a phosphorus meteoric input function. The estimated global mean P deposition flux, in the form of sub-micron sized meteoric smoke particles, is $1 \times 10^{-8} \text{ g m}^{-2} \text{ yr}^{-1}$, with a maximum of $\sim 5 \times 10^{-8} \text{ g m}^{-2} \text{ yr}^{-1}$ over the northern Rockies, Himalayas and southern Andes. The estimated fraction of ablated phosphorus forming bio-available metal phosphites is 11%, which results from the very large concentrations of O and H compared to OH in the upper mesosphere. A layer of OPO is predicted to occur at 90 km with a peak of concentration of $\sim 50 \text{ cm}^{-3}$; this is the counterpart of the well-known layers of meteoric metals such as Na and Fe, and may be observable spectroscopically.

1. Introduction

Phosphorus is a key element in biomolecules (e.g. RNA, DNA, phospholipids, ATP/ADP) and therefore plays important roles in replication, information transfer, and metabolism [Maciá, 2005]. Although the dominant form of inorganic P at the Earth’s surface is orthophosphate (PO_4^{3-} , oxidation state +5), phosphate salts have low water solubility and reactivity, which severely limits their bio-availability. Therefore, a major question concerning the development of early life on Earth was the availability of pre-biotic P in its reduced forms, phosphides (P^- , oxidation state -1), phosphites (HPO_3^{2-} , oxidation state +3) or hypophosphites (H_2PO_2^- , oxidation state +3), which are more biologically active than the fully oxidized phosphate. Phosphorus is thought to have limited ocean primary productivity over geological timescales, and the P cycle may have constrained the slow oxygenation of the Earth’s surface during the first 3.5 billion years [Lyons *et al.*, 2014]. In support of this hypothesis of P bio-limitation, Reinhard *et al.* [2017] have shown recently that until around 800 million years ago the P in shallow marine environments was significantly lower than the Redfield ratio [Redfield, 1958].

Because phosphorus is a siderophile element, the P that was present when the Earth formed should be sequestered in the molten core; hence, extra-terrestrial P was probably the major source of pre-biotic phosphorus at the planet’s surface [Pasek, 2008]. Previous studies have focused on the direct delivery of P to the surface in meteorites, where metal phosphides (in particular the mineral schreibersite, $(\text{FeNi})_3\text{P}$) were then processed into bio-available forms of P through aqueous-phase chemistry [Pasek, 2008; Gibard *et al.*, 2019]. A very recent study has shown that cloud-ground lightning strikes reduce phosphate in meteorites, and estimated that lightning strikes on early Earth might have formed 10–1000 kg of phosphide and 100–10,000 kg of phosphite and hypophosphite annually [Hess *et al.*, 2021].

In the present paper we consider the ablation of P from interplanetary dust particles (IDPs) entering the Earth’s atmosphere and its subsequent atmospheric chemistry. This potential source of reduced P does not appear to have been investigated previously. Most IDPs have a mass ranging from 10^{-3} to 100 g (radius 2 - 200 μm), and a substantial fraction of the IDP mass ablates due to aerobraking at heights between 70 and 110 km [Carrillo-Sánchez *et al.*, 2020b]. We recently performed a laboratory study of phosphorus ablation from μm -size meteoritic particles, which were flash heated to temperatures as high as 2900 K in a Meteoric Ablation Simulator (MASI), and the ablation of PO and Ca recorded simultaneously by laser induced fluorescence [Carrillo-Sánchez *et al.*, 2020a]. In the same study we showed using XANES spectroscopy that phosphorus in anhydrous chondritic porous IDPs mainly occurs in phosphate-like domains. A thermodynamic model of phosphorus in a silicate melt was then developed for inclusion in the Leeds Chemical Ablation Model (CABMOD) [Vondrak *et al.*, 2008]. This model satisfactorily reproduces the PO and Ca ablation profiles observed in the MASI, correctly predicting that meteoritic P is moderately volatile (similar to Fe) compared with the more refractory Ca. The speciation of ablated P is sensitive to the oxygen fugacity, and P should mainly be injected into the

Earth’s atmosphere as OPO, which then likely undergoes dissociation to PO (and perhaps to P and P^+), through hyperthermal collisions with air molecules. The global input of ablated P to the atmosphere was estimated to be 6200 kg yr^{-1} [Carrillo-Sánchez *et al.*, 2020a].

The vaporized phosphorus species will then undergo chemical processing to form a variety of compounds in which P may exist in different oxidation states due to the presence of both oxidizing and reducing agents in the upper atmosphere. In Section 2 of this paper we develop a network of P atmospheric chemistry reactions. This involves combining our recent laboratory kinetic studies of the reactions of P, PO and OPO [Douglas *et al.*, 2019; Douglas *et al.*, 2020] with theoretical estimates of the rate coefficients of reactions not yet studied experimentally; these are determined using high-level electronic structure calculations to determine energetically viable reaction pathways and then applying statistical rate theory. In Section 3 the P chemical network is incorporated into a global chemistry-climate model. As discussed in Section 4, the model results indicate that in the present-day atmosphere about 11% of the P entering the atmosphere should be deposited at the surface in the reduced form of biologically-active metal phosphites.

2. Phosphorus atmospheric chemistry

2016] to determine the nature of the potential energy surface (PES). The vibrational frequencies, rotational constants and energies of the stationary points (i.e. reactants, intermediates, transition states and products) of each reaction were calculated with the Complete Basis Set (CBS-QB3) method [Montgomery *et al.*, 1999]. Tables S1 – S9 in the Supporting Information (SI) list the Cartesian coordinates, molecular parameters and heats of formation of the relevant neutral phosphorus species.

Rice-Ramsperger-Kassel-Markus (RRKM) calculations were then performed for each reaction using the Master Equation Solver for Multi-Energy well Reactions (MESMER) program [Glowacki *et al.*, 2012]. Each reaction is assumed to proceed via the formation of an excited adduct, which can either dissociate or be stabilized by collision with the N_2 third body. The internal energy of this adduct was divided into a contiguous set of grains (typical width 50 cm^{-1}) containing a bundle of rovibrational states. Each grain was then assigned a set of microcanonical rate coefficients for dissociation to reactants or products (where appropriate). These were determined using inverse Laplace transformation to link them directly to $k_{\text{rec},\infty}$, the high pressure limiting recombination coefficient for the forward or reverse reaction. $k_{\text{rec},\infty}$ was set to $5 \times 10^{-10} (T/300)^{0.167} \text{ cm}^3 \text{ molecule}^{-1} \text{ s}^{-1}$, typical of the capture rate coefficient for a reaction governed by long-range dispersive and ion-induced dipole forces [Georgievskii and Klippenstein, 2005]. The density of states of each adduct was calculated with the vibrational frequencies and rotational constants listed in Tables S1 – S9, without making a correction for anharmonicity, and a classical densities of states treatment for the rotational modes. The microcanonical rate coefficients for reactions over barriers were treated using RRKM theory, with Eckart tunnelling applied where an H atom transfer occurred [Glowacki *et al.*, 2012]. The probability of collisional transfer between grains following collision with air molecules (treated here as N_2) was estimated using the exponential down model; the average energy for downward transitions, $\langle E \rangle_{\text{down}}$, was set to 300 cm^{-1} at 300 K with a small $T^{0.25}$ temperature dependence, and the probabilities for upward transitions determined by detailed balance [Gilbert and Smith, 1990]. The collision rate of N_2 with the adduct as a function of temperature was calculated using Lennard-Jones parameters ($\sigma = 3.0\text{ \AA}$ and $\epsilon = 200\text{ cm}^{-1}$) to characterise the intermolecular potential. The Master Equation (which describes the evolution with time of the adduct grain populations) was then expressed in matrix form and solved to yield the rates of the various possible reaction channels (i.e. recombination and/or bimolecular reaction), at a specified pressure and temperature.

2.1 Neutral chemistry

The initial oxidation of P will proceed *via* successive oxidation by O_2 to produce OPO (reactions R1 and R2 below) [Douglas *et al.*, 2019; Douglas *et al.*, 2020]. O_3 probably also plays an analogous role to O_2 in oxidizing P to OPO, but the O_3/O_2 ratio in the MLT is only around 10^{-5} so its role will be very minor. OPO can then be oxidized to PO_3 by the very exothermic reaction with O_3 (R3) [Douglas *et al.*, 2020]. However, PO_3 is reduced back to OPO by reaction

with O and H (R4 and R5). There is a submerged barrier on the $\text{PO}_3 + \text{O}$ PES (87 kJ mol^{-1} below the reactants – see Table S5). This reaction should therefore proceed close to the collision frequency between PO_3 and O, divided by a statistical factor of 2 to take account of the fact that only the PES of doublet spin multiplicity is reactive (the reaction involve reactants with doublet (PO_3) and triplet (O) spin multiplicities and can therefore proceed on surfaces of doublet or quartet multiplicity). There is no barrier on the $\text{PO}_3 + \text{H}$ PES.

$$\Delta H_{(0 \text{ K})} (\text{kJ mol}^{-1})$$

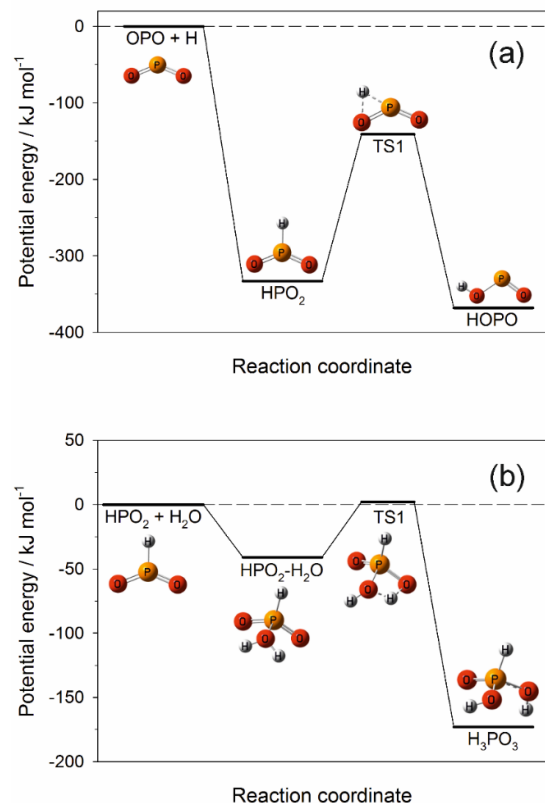
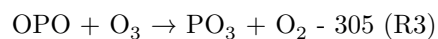
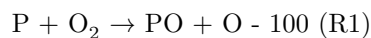


Figure 2. Potential energy surfaces calculated at the CBS-QB3 level of the

theory [Montgomery *et al.*, 1999]: (a) $\text{OPO} + \text{H}$ forming HPO_2 or HOPO ; (b) HPO_2 recombining with H_2O to form H_3PO_3 (phosphonic acid).

In the MLT, OPO is therefore likely to recombine with H to form either HPO_2 or HOPO (R6a or R6b), on the PES illustrated in Figure 2. R6a is the slightly less exothermic channel, and so 11% of the product is predicted to be HPO_2 at 200 K (a temperature typical of the MLT). As shown by the green arrows in Figure 1, the route to H_3PO_3 (phosphonic acid) then requires the recombination of HPO_2 with H_2O (R7), on the PES illustrated in Figure 2(b). This reaction involves formation of an $\text{HPO}_2\text{-H}_2\text{O}$ complex which then rearranges over an essentially thermoneutral barrier to H_3PO_3 .

H_3PO_4 (phosphoric acid) is formed via HOPO_2 , the P-analogue of nitric acid (major pathways depicted with red arrows in Figure 1). HOPO_2 can form by recombination of OPO with OH (R8). However, the more important route is through the bimolecular reaction of OH with HOPO (R9). The PES for this reaction, illustrated in Figure 3a, shows that the alternative pathway to $\text{OPO} + \text{H}_2\text{O}$ involves a barrier of 8 kJ mol^{-1} . HOPO_2 can also form via reaction of HPO_2 with OH (R10a). The PES for R10 is shown in Figure S1. The reaction channel forming HOPO is minor (8% at 200 K), and OPO formation is insignificant. H_3PO_4 then forms by recombination of HOPO_2 with H_2O (R11). The PES for this reaction (Figure 3b) shows that formation of a $\text{HOPO}_2\text{-H}_2\text{O}$ complex is followed by rearrangement over a thermoneutral barrier to H_3PO_4 . Alternatively, H_3PO_4 can form by the sequential addition of H and OH (R12 and R13), though this is a less important route (see Section 4).

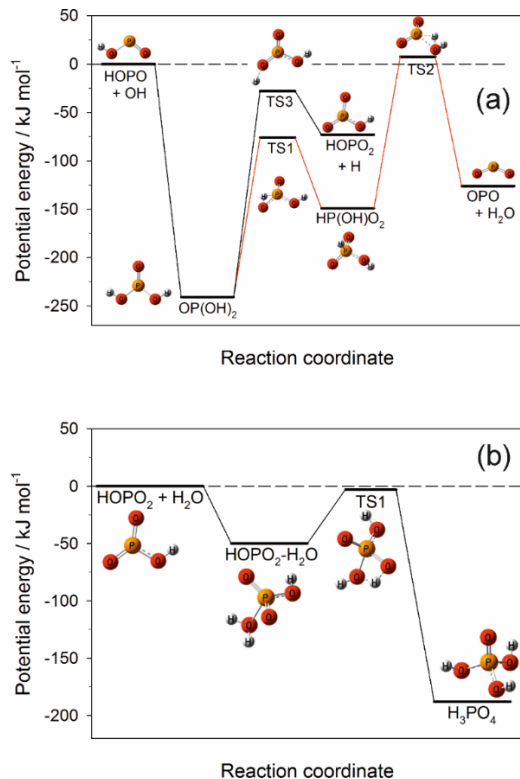
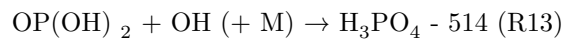
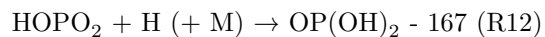
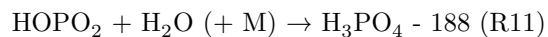
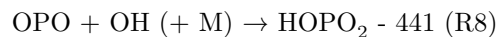
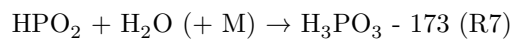
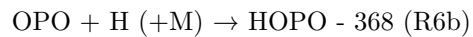
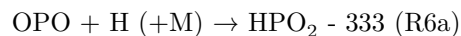


Figure 3. Potential energy surfaces calculated at the CBS-QB3 level of the theory [Montgomery *et al.*, 1999]: (a) $\text{HOPO} + \text{OH}$ to form HOPO_2 (black route) or $\text{OPO} + \text{H}_2\text{O}$ (red route); (b) HOPO_2 recombining with H_2O to form H_3PO_4 (phosphoric acid).

$$\Delta H_{(0\text{ K})} (\text{kJ mol}^{-1})$$



Other reactions which cycle between $\text{OP}(\text{OH})_2$, $\text{HP}(\text{O})\text{OH}$, HOPO_2 , HOPO and HPO_2 are illustrated in Figure 1, and their rate coefficients listed in Table 1 (R14 – R20). These reactions involve the species O, H and OH. Note that since these species have relative abundances of $\sim 10^6 : 10^3 : 1$ above 80 km [Plane *et al.*, 2015], the OH reactions play a minor role. The PES for the reaction between $\text{HP}(\text{O})\text{OH}$ and O has four bimolecular reaction channels (Figure S2), though formation of OPO is the major channel (63% at 200 K).

Once H_3PO_3 and H_3PO_4 form, they appear to be stable with respect to mesospheric constituents such as H, O and OH (their photochemistry is discussed below in Section 2.4). In the case of H_3PO_3 reacting with H, the pathway forming $\text{OP}(\text{OH})_2 + \text{H}_2$ is exothermic by 46 kJ mol⁻¹, but has a barrier of 28 kJ mol⁻¹; and the pathway forming $\text{HP}(\text{OH})\text{O}_2 + \text{H}_2$ is endothermic by 45 kJ mol⁻¹ and has a barrier of 95 kJ mol⁻¹. The reaction of O with H_3PO_3 to form $\text{OP}(\text{OH})_2 + \text{OH}$ is exothermic by 35 kJ mol⁻¹, but has a barrier of 24 kJ mol⁻¹; the pathway forming $\text{HP}(\text{OH})\text{O}_2 + \text{OH}$ is endothermic by 56 kJ mol⁻¹ and has a barrier of 79 kJ mol⁻¹; and although recombination of O with H_3PO_3 to form H_3PO_4 is potentially highly exothermic (by 549 kJ mol⁻¹) it would involve a non-adiabatic switch from the initial triplet surface (as well as insertion of the O into the H-P bond). The reaction of OH with H_3PO_3 to form $\text{OP}(\text{OH})_2 + \text{H}_2\text{O}$ is exothermic by 102 kJ mol⁻¹, but has a barrier of 9 kJ mol⁻¹; the pathway forming $\text{HP}(\text{OH})\text{O}_2 + \text{H}_2\text{O}$ is exothermic by 11 kJ mol⁻¹ but has a barrier of 44 kJ mol⁻¹; and the reaction to form $\text{H}_3\text{PO}_4 + \text{H}$ is exothermic by 123 kJ mol⁻¹ but has a barrier of 20 kJ mol⁻¹. Since there does not appear to be a low temperature route to form $\text{HP}(\text{OH})\text{O}_2$ from H_3PO_3 , $\text{HP}(\text{OH})\text{O}_2$ is not shown in Figure 1.

In the case of H_3PO_4 , reaction with H to form $\text{OP}(\text{OH})_2 + \text{H}_2\text{O}$ or $\text{OP}(\text{OH})_2\text{O} + \text{H}_2$ are endothermic by 21 and 45 kJ mol⁻¹, respectively; reaction with OH to form $\text{OP}(\text{OH})_2\text{O} + \text{H}_2\text{O}$ is exothermic by 12 kJ mol⁻¹ but has a barrier of 24 kJ mol⁻¹; and reaction with O to form $\text{H}_3\text{PO}_3 + \text{O}_2$ is endothermic by 52 kJ mol⁻¹. $\text{HP}(\text{OH})\text{O}$ is therefore omitted from Figure 1.

2.2 Ion-molecule chemistry

The ion-molecule chemistry of phosphorus is comparatively unimportant. This is because P^+ ions react rapidly with O_2 (and CO_2 , R22) to produce PO^+ (R21) [Anicich, 2003]. This reaction is highly exothermic even if the O is produced in the singlet excited state to conserve spin on a singlet surface:



P-containing ions can be formed either directly during ablation [Carrillo-Sánchez *et al.*, 2020a], or via exothermic charge transfer reactions (R23 – R26) between P, PO and OPO and the ambient ions NO^+ and O_2^+ in the lower *E* region (90 – 150 km). Note that the reaction between P and O_2^+ could also make $\text{PO}^+ + \text{O}$ directly (exothermic by 453 kJ mol⁻¹), though P should be a very minor species because the rate of R1 is so high. OPO^+ can be reduced back to PO^+ by O:



However, the reaction of PO^+ with O is very endothermic (by 301 kJ mol^{-1} , or 395 kJ mol^{-1} , if spin is conserved to produce $\text{P}^+ + \text{O}_2(\text{a}^1_{\text{g}})$). In contrast, the meteor-ablated metallic ions such as Fe^+ and Mg^+ can only form their comparatively weakly bound oxides FeO^+ and MgO^+ by reaction with O_3 rather than O_2 , and these oxides are very rapidly reduced back to the atomic ions by reaction with the large excess of O in the lower thermosphere [Plane *et al.*, 2015]. Atomic ions can only be neutralised by the relatively slow process of dielectronic (or radiative) recombination with electrons, which allows significant concentrations of metallic atomic ions to occur above 90 km in the atmosphere [Plane *et al.*, 2015]. In contrast, molecular ions such as PO^+ and OPO^+ will undergo much faster dissociative recombination reactions (R28 and R29), and the concentrations of these ions should be relatively small in the MLT.

2.3 Photochemistry

The photolysis rates of H_3PO_3 , H_3PO_4 , HOPO_2 , HPO_2 and HOPO were estimated by using time-dependent density function theory (TD-DFT) [Bauernschmitt and Ahlrichs, 1996]. The vertical excitation energies and transition dipole moments for transitions from the ground state of each molecule up to the first 30 electronically excited states were calculated to produce the absorption cross sections shown in Figure 4. Each cross section was then convolved up to its dissociation threshold with the solar actinic flux from the SOLAR2000 empirical solar irradiance model [Tobiska *et al.*, 2000] (averaged over a solar cycle). The resulting photodissociation reactions are shown in Table 1 (R30 – R34). The photolysis threshold was set to correspond to the lowest bond dissociation energy at the CBS-QB3 level of theory. These thresholds, indicated with arrows in Figure 4, are an upper wavelength limit because a photon with more than the bond energy may be required depending on the position of the upper dissociating electronic states.

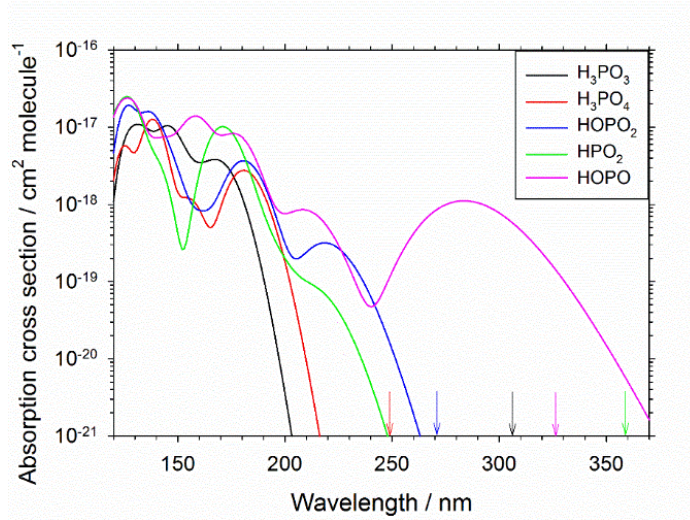


Figure 4. Absorption cross sections of H_3PO_3 , H_3PO_4 , HOPO_2 , HPO_2 and HOPO computed at the TD//B3LYP/6-311+g(2d,p) level of theory [Frisch *et al.*, 2016]. The vertical arrows indicate upper limits to the photolysis thresholds, computed from the relevant bond dissociation energies at the CBS-QB3 level of theory [Montgomery *et al.*, 1999].

Figure 4 shows that the absorption cross section of H_3PO_3 (black line) only starts to become significant below 200 nm, and so it has the lowest photodissociation rate of $5.0 \times 10^{-6} \text{ s}^{-1}$. HOPO , in contrast, can potentially photolyse below 327 nm where it already has a large absorption cross section, and so its photodissociation rate is estimated to be $2.8 \times 10^{-3} \text{ s}^{-1}$ (Table 1).

2.4 Incorporation into meteoric smoke particles

Reactions R35 - R38 in Table 1 are condensation reactions (i.e. acid + base \rightarrow salt + H_2O) of H_3PO_3 and H_3PO_4 with alkaline metal-containing molecules represented here as FeOH and $\text{Fe}(\text{OH})_2$, which are reservoir species for meteor-ablated Fe below the atomic Fe layer centred around 86 km [Feng *et al.*, 2013]. Fe is the most abundant meteoric metal, followed by Mg and Na. Their major molecular reservoirs [Plane *et al.*, 2015] all undergo exothermic condensation reactions with the acidic H_3PO_3 and H_3PO_4 :

$$\Delta H_{(0 \text{ K})} \text{ (kJ mol}^{-1}\text{)}$$





The resulting metal phosphite and phosphate molecules are illustrated in Figure S3. As shown in Table 1, the rate coefficients $k_{35} - k_{38}$ are set to $1 \times 10^{-9} \text{ cm}^3 \text{ molecule}^{-1} \text{ s}^{-1}$. This represents a typical rate coefficient of $5 \times 10^{-10} \text{ cm}^3 \text{ molecule}^{-1} \text{ s}^{-1}$ for long-range capture involving molecules with permanent dipole moments (hence the absence of a significant temperature dependence) [Georgievskii and Klippenstein, 2005], multiplied by a factor of 2 to take account of the fact that Fe is ~48% of the total ablated meteoric metals (Fe + Mg + Na) [Carrillo-Sánchez et al., 2020b]. The metal phosphites/phosphates produced by R35 – R38 are assumed to be phosphorus sinks, and these become incorporated into meteoric smoke particles (MSPs), the nm-sized particles which form in the MLT from the polymerization of meteoric metal compounds [Plane et al., 2015].

Table 1. Phosphorus chemistry in the MLT

No.	Reaction	Rate coefficient ^a
<i>Neutral reactions</i>		
R1	$\text{P} + \text{O}_2 \rightarrow \text{PO} + \text{O}$	$k_1 = 3.08 \times 10^{-13} (T/298)^{2.24 \text{ b}}$
R2	$\text{PO} + \text{O}_2 \rightarrow \text{OPO} + \text{O}$	$k_2 = 1.42 \times 10^{-11} (T/298)^{0.305 \text{ b}}$
R3	$\text{OPO} + \text{O}_3 \rightarrow \text{PO}_3 + \text{O}_2$	$k_3 = 3.72 \times 10^{-11} \exp(-1131/T) \text{ c}$
R4	$\text{PO}_3 + \text{O} \rightarrow \text{OPO} + \text{O}_2$	$k_4 = 4.01 \times 10^{-11} (T/298)^{-0.04 \text{ d}}$
R5	$\text{PO}_3 + \text{H} \rightarrow \text{OPO} + \text{OH}$	$k_5 = 2 \times 10^{-10} (T/298)^{0.5 \text{ e}}$
R6a	$\text{OPO} + \text{H} (+ \text{N}_2) \rightarrow \text{HPO}_2$	$k_{6a} = 2.01 \times 10^{-28} (T/298)^{-2.31 \text{ d}}$
R6b	$\text{OPO} + \text{H} (+ \text{N}_2) \rightarrow \text{HOPO}$	$k_{6b} = 1.26 \times 10^{-27} (T/298)^{-2.93 \text{ d}}$
R7	$\text{HPO}_2 + \text{H}_2\text{O} (+ \text{N}_2) \rightarrow \text{H}_3\text{PO}_3$	$k_7 = 5.09 \times 10^{-28} (T/298)^{0.883 \text{ d}}$
R8	$\text{OPO} + \text{OH} (+ \text{N}_2) \rightarrow \text{HOPO}_2$	$k_8 = 5.63 \times 10^{-27} (T/298)^{-3.56 \text{ d}}$
R9	$\text{HOPO} + \text{OH} \rightarrow \text{HOPO}_2 + \text{H}$	$k_9 = 6.21 \times 10^{-11} (T/298)^{-1.25 \text{ d}}$
R10a	$\text{HPO}_2 + \text{OH} \rightarrow \text{HOPO}_2 + \text{H}$	$k_{10a} = 8.81 \times 10^{-11} (T/298)^{0.010 \text{ d}}$
R10b	$\text{HPO}_2 + \text{OH} \rightarrow \text{HOPO} + \text{OH}$	$k_{10b} = 8.96 \times 10^{-12} (T/298)^{0.363 \text{ d}}$
R11	$\text{HOPO}_2 + \text{H}_2\text{O} (+ \text{N}_2) \rightarrow \text{H}_3\text{PO}_4$	$\log_{10}(k_{11}) = -13.290 - 10.378 \log_{10}(T) + 1.9723(\log_{10}(T))^2 \text{ d}$
R12	$\text{HOPO}_2 + \text{H} (+ \text{N}_2) \rightarrow \text{OP}(\text{OH})_2$	$k_{12} = 5.85 \times 10^{-25} (T/298)^{0.358 \text{ d}}$
R13	$\text{OP}(\text{OH})_2 + \text{OH} (+ \text{N}_2) \rightarrow \text{H}_3\text{PO}_4$	$\log_{10}(k_{13}) = -36.906 + 23.3622 \log_{10}(T) - 4.9468 (\log_{10}(T))^2 \text{ d}$
R14	$\text{HPO}_2 + \text{H} \rightarrow \text{OPO} + \text{H}_2$	$k_{14} = 5.42 \times 10^{-11} \exp(-1548/T) \text{ d}$
R15	$\text{HOPO} + \text{H} (+ \text{N}_2) \rightarrow \text{HP}(\text{O})\text{OH}$	$k_{15} = 1.22 \times 10^{-28} (T/298)^{-3.13 \text{ d}}$
R16	$\text{OP}(\text{OH})_2 + \text{H} \rightarrow \text{HOPO}_2 + \text{H}_2$	$k_{16} = 2 \times 10^{-10} (T/298)^{0.5 \text{ e}}$
R17	$\text{OP}(\text{OH})_2 + \text{O} \rightarrow \text{HOPO}_2 + \text{OH}$	$k_{17} = 2 \times 10^{-10} (T/298)^{0.5 \text{ e}}$
R18	$\text{HP}(\text{O})\text{OH} + \text{H} \rightarrow \text{HOPO} + \text{H}_2$	$k_{18} = 2 \times 10^{-10} (T/298)^{0.5 \text{ e}}$
R19a	$\text{HP}(\text{O})\text{OH} + \text{O} \rightarrow \text{OPO} + \text{H}_2\text{O}$	$k_{19a} = 1.20 \times 10^{-10} (T/298)^{0.125 \text{ d}}$

No.	Reaction	Rate coefficient ^a
R19b	HP(O)OH + O → HOPO ₂ + H	$k_{19b} = 2.94 \times 10^{-11} (T/298)^{-0.028}$ ^d
R19c	HP(O)OH + O → HPO ₂ + OH	$k_{19c} = 1.90 \times 10^{-11} (T/298)^{-0.018}$ ^d
R19d	HP(O)OH + O → HOPO + OH	$k_{19d} = 1.73 \times 10^{-11} (T/298)^{-0.08}$ ^d
R20	HP(O)OH + OH → HOPO + H ₂ O	$k_{20} = 2 \times 10^{-10} (T/298)^{0.5}$ ^e
<i>Ion-molecule reactions</i>		
R21	P ⁺ + O ₂ → PO ⁺ + O	$k_{21} = 5.30 \times 10^{-10}$ ^f
R22	P ⁺ + CO ₂ → PO ⁺ + CO	$k_{22} = 4.90 \times 10^{-10}$ ^f
R23	P + O ₂ ⁺ → P ⁺ + O ₂	$k_{23} = 1 \times 10^{-9}$ ^g
R24	PO + NO ⁺ → PO ⁺ + NO	$k_{24} = 1 \times 10^{-9}$ ^g
R25	PO + O ₂ ⁺ → PO ⁺ + O ₂	$k_{25} = 1 \times 10^{-9}$ ^g
R26	OPO + O ₂ ⁺ → OPO ⁺ + O ₂	$k_{26} = 1 \times 10^{-9}$ ^g
R27	OPO ⁺ + O → PO ⁺ + O ₂	$k_{27} = 3 \times 10^{-10}$ ^g
R28	OPO ⁺ + e ⁻ → PO + O	$k_{28} = 3 \times 10^{-7} (T/298)^{-0.5}$ ^h
R29	PO ⁺ + e ⁻ → P + O	$k_{29} = 3 \times 10^{-7} (T/298)^{-0.5}$ ^h
<i>Photochemical reactions</i>		
R30	HOPO + <i>hν</i> → H + OPO	$J_{30} = 2.8 \times 10^{-3}$ ⁱ
R31	HPO ₂ + <i>hν</i> → H + OPO	$J_{31} = 5.0 \times 10^{-5}$ ⁱ
R32	H ₃ PO ₃ + <i>hν</i> → OP(OH) ₂ + H	$J_{32} = 5.0 \times 10^{-6}$ ⁱ
R33	H ₃ PO ₄ + <i>hν</i> → OP(OH) ₂ + OH	$J_{33} = 1.4 \times 10^{-5}$ ⁱ
R34	HOPO ₂ + <i>hν</i> → OH + OPO	$J_{34} = 6.1 \times 10^{-5}$ ⁱ
<i>Condensation reactions</i>		
R35	H ₃ PO ₃ + FeOH → MSP-PO ₃	$k_{35} = 1 \times 10^{-9}$ ^j
R36	H ₃ PO ₃ + Fe(OH) ₂ → MSP-PO ₃	$k_{36} = 1 \times 10^{-9}$ ^j
R37	H ₃ PO ₄ + FeOH → MSP-PO ₄	$k_{37} = 1 \times 10^{-9}$ ^j
R38	H ₃ PO ₄ + Fe(OH) ₂ → MSP-PO ₄	$k_{38} = 1 \times 10^{-9}$ ^j

^a Units: s⁻¹ for photolysis reactions; cm³ molecule⁻¹ s⁻¹ for bimolecular reactions; cm⁶ molecule⁻² s⁻¹ for termolecular reactions. ^b *Douglas et al.* [2019]. ^c [*Douglas et al.*, 2020]. ^d RRKM Master Equation calculation (see text). ^e set to a typical collision frequency, since the reaction is barrierless. ^f *Anicich* [2003]. ^g Set to a typical value for charge exchange with these molecular ions [*Plane et al.*, 2015]. ^h Set to a typical value for the dissociative recombination of a small molecular ion with an electron [*Florescu-Mitchell and Mitchell*, 2006]. ⁱ Calculated at the TD//B3LYP/6-311+g(2d,p) level of theory (see text). ^j See text.

3. Global modelling of phosphorus in the MLT region

3.1 WACCM-P set up

The phosphorus reactions in Table 1 were imported into the Whole Atmosphere Community Climate Model (WACCM) [*Gettelman et al.*, 2019] from the US National Center for Atmospheric Research. We have previously used this global chemistry-climate model to study the atmospheric chemistries of various meteor-ablated metals including Fe [*Feng et al.*, 2013], Mg [*Langowski et al.*, 2015] and Na [*Marsh et al.*, 2013]. The version we employ here, WACCM6 [*Gettelman et*

et al., 2019], uses the framework developed from the second iteration of the fully coupled Community Earth System Model (CESM2) [Danabasoglu *et al.*, 2020]. The model extends vertically from the surface to the lower thermosphere at ~ 140 km. In the present study we used the free-running (FR) version of WACCM because there are no observations of P species against which to compare the simulations (and the FR version simulates Fe and Fe^+ satisfactorily [Feng *et al.*, 2013]). The model has a horizontal resolution of 1.9° latitude \times 2.5° longitude, and 70 vertical model layers (3.5 km vertical resolution in the MLT region). This version of WACCM6 with phosphorus chemistry is termed here WACCM-P. The full set of Fe reactions in WACCM-Fe [Feng *et al.*, 2013; Viehl *et al.*, 2016] was also included in order to produce the FeOH and $\text{Fe}(\text{OH})_2$ required for R35 – R38. The model simulations were performed from 2004 to 2014 using the standard WACCM6 initialization conditions file [Danabasoglu *et al.*, 2020], following a 5 year spin-up with Fe and P chemistry. This 11-year period is sufficiently long to produce a climatology of the phosphorus species.

3.2 The phosphorus meteoric input function

Figure 5 shows the global average injection profiles of PO and Fe used in WACCM. Note that although ~ 6 times more OPO than PO should ablate [Carrillo-Sánchez *et al.*, 2020a], most of the OPO will then be converted immediately to PO through hyperthermal collisions with N_2 or O_2 . The PO profile shown here is therefore the total phosphorus input. These Meteoric Input Functions (MIFs) were estimated by combining the new version of the Chemical Ablation Model (CABMOD-3), which simulates the ablation of the major meteoric elements and OPO/PO/P from an individual dust particle [Carrillo-Sánchez *et al.*, 2020a; Carrillo-Sánchez *et al.*, 2020b], with the Zodiacal Cloud Model (ZoDY) which provides the mass, velocity and radiant distributions of particles entering the atmosphere. ZoDY contains contributions from different dust sources: Jupiter Family Comets, the asteroid belt, and long-period Halley-Type comets [Nesvorný *et al.*, 2011], which are weighted using the procedure described in Carrillo-Sánchez *et al.* [2016]. The PO and Fe injection height-profiles in Figure 5 are similar in shape, peaking around 94 km. The ratio of the PO:Fe injection rates is ~ 0.01 between 70 and 140 km, which is close to their relative elemental abundance in meteorites of 9.6×10^{-3} [Asplund *et al.*, 2009] multiplied by their relative ablation efficiency of 1.13 [Carrillo-Sánchez *et al.*, 2020a]. The secondary peak around 108 km in both injection profiles arises from fast meteors (mostly from Halley-Type comets), and the lower peaks from slow meteors (mostly from Jupiter Family comets and asteroidal particles).

The PO and Fe injection profiles in Figure 5 have been reduced by a factor of 5 from the profiles predicted by the CABMOD-ZoDY model [Carrillo-Sánchez *et al.*, 2020a; Carrillo-Sánchez *et al.*, 2020b]. This is a standard procedure that we have adopted to allow for the fact that vertical transport of minor species in the MLT tends to be underestimated in global models such as WACCM6 [Plane *et al.*, 2018; Daly, 2020]. The “missing” transport arises because short wavelength gravity waves are not resolved on the current horizontal grid scale of

the model (~ 220 km), and these sub-grid waves contribute to vertical chemical and dynamical transport of constituents while dissipating [Gardner *et al.*, 2017]. In order to correctly simulate the observed *absolute* densities of species such as Fe, Na and Ca when vertical transport is underestimated, the MIF of each species needs to be reduced by this factor of ~ 5 [Plane *et al.*, 2018; Daly, 2020]. The PO MIF is then set to vary with season and latitude in the same way as the Fe MIF [Feng *et al.*, 2013] i.e. an autumnal maximum and vernal minimum, increasing from essentially no variation at the equator to $\pm 30\%$ at the pole, with the same annual average input at all latitudes.

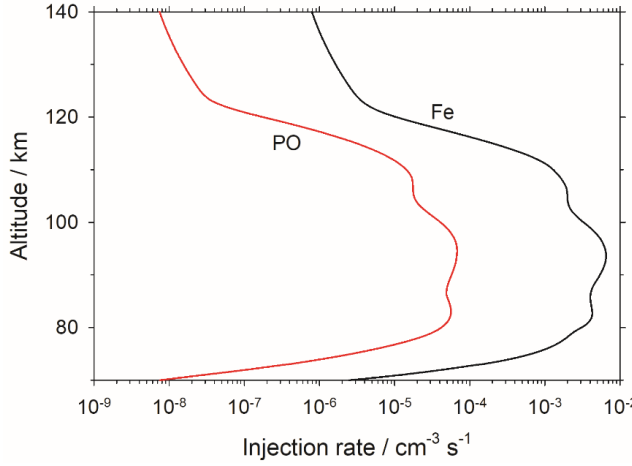


Figure 5. Global annual mean injection rates of PO (representing P + PO + OPO) and Fe from meteoric ablation. The injection profiles predicted by the CABMOD-ZoDY model [Carrillo-Sánchez *et al.*, 2020a; Carrillo-Sánchez *et al.*, 2020b] have been divided by a factor of 5.0 for input into the WACCM6 model (see text).

4. Discussion

Figure 6 illustrates the results of three WACCM-P runs which explore the role of photolysis and MSP formation. The panels show the vertical profiles of the P-containing species, averaged over 11 years (2004 - 2014) at mid-latitudes (54°N). For all three model experiments, the P ions are very minor species, occurring in a layer that peaks around 95 km with a peak concentration of only $7 \times 10^{-2} \text{ cm}^{-3}$. This result was anticipated in Section 3.2: P^+ ions are overwhelmingly converted to molecular PO^+ by reaction with O_2 or CO_2 , which then undergoes rapid dissociative recombination with electrons. This is consistent with the absence of P^+ in rocket-borne mass spectrometric measurements in the Earth’s lower E region [Kopp *et al.*, 1985; Grebowsky and Aikin, 2002], and measurements with the Neutral Gas Ion Mass Spectrometer (NGIMS) instrument on the MAVEN satellite orbiting Mars, where the atomic ions of less abundant meteoric species

(e.g. K^+ , Ti^+ , Cu^+) were observed [Benna *et al.*, 2015].

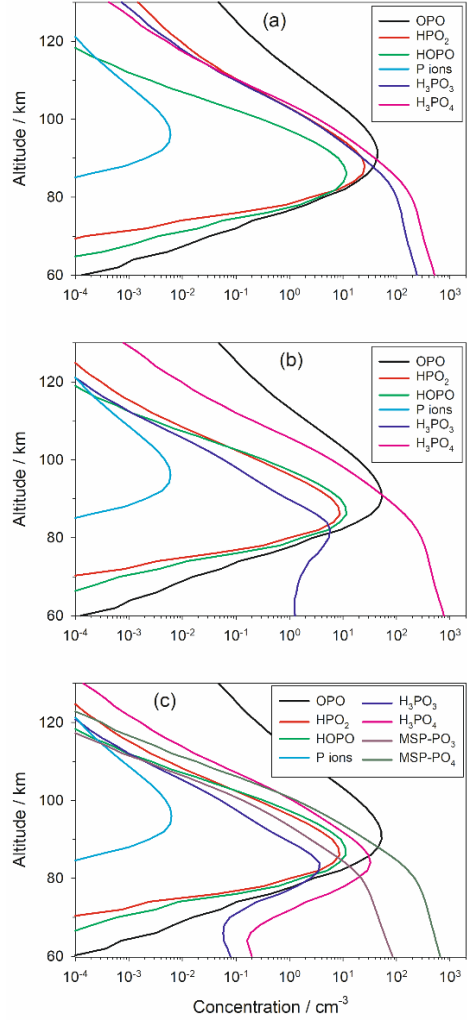


Figure 6. Mean vertical profiles of P-containing species averaged over 11 years (2004 -2014) at mid-latitudes ($54^\circ N$) : (a) Photolysis of P species (R34 - R38) turned off and MSP-forming condensation reactions (R30 - R33) turned off; (b) Photolysis (R34 - R38) turned on, MSP formation (R30 - R33) turned off; (c) Photolysis and MSP formation turned on (i.e. full P chemistry R1 – R38 turned on).

The three panels in Figure 6 show that above 90 km the major P-containing species is OPO, which occurs in a broad layer peaking around 90 km, with a full width at half maximum (FWHM) of ~ 14 km. HPO_2 and HOPO also occur in layers which peak around 86 km, since they are produced by the pressure-

dependent recombination of OPO with H (R6a and b). P, PO, HOPO₂ and PO₃ are very minor, with a combined total concentration of less than 0.02 cm⁻³.

The only other important neutral species are H₃PO₃ and H₃PO₄. In Figure 6a where there is no photolysis or MSP formation, they become the dominant species below 86 km since they represent the two phosphorus sinks (Figure 1). The H₃PO₃ : H₃PO₄ ratio is ~0.5 below 86 km. However, when photolysis is turned on (Figure 6b), H₃PO₃ is significantly depleted and the ratio becomes less than 0.01. The reason for this is that, although the H₃PO₃ photodissociation rate is relatively small (Section 2.3), the lowest energy dissociation channel of H₃PO₃ produces OP(OH)₂ + H (R32), and OP(OH)₂ can then form H₃PO₄ (Figure 1). It should be kept in mind that production of OP(OH)₂ from H₃PO₃ may not be the dominant photodissociation pathway: H₃PO₃ only absorbs significantly below 200 nm (Figure 4) where the photon energy is sufficient to produce HP(OH)O₂ + H (threshold = 482 kJ mol⁻¹, < 248 nm) or HP(O)OH + OH (threshold = 482 kJ mol⁻¹, < 240 nm).

Figure 6c shows the effect of including both photolysis and the condensation reactions with FeOH and Fe(OH)₂ to produce metal phosphites (labelled MSP-PO₃) and phosphates (MSP-PO₄). Because the total concentration of the metal hydroxides/carbonates is more than 2×10^4 cm⁻³ below 85 km [Feng *et al.*, 2013; Marsh *et al.*, 2013; Plane *et al.*, 2015], the condensation reactions of H₃PO₃ and H₃PO₄ are relatively rapid and MSP-PO₃ and MSP-PO₄ become the dominant forms of phosphorus below 85 km, with a ratio of 0.11.

The OPO layer is the counterpart to the layers of metal atoms such as Na and Fe which have been observed for decades by the ground-based lidar technique [Plane *et al.*, 2015], and the layer of SiO that is predicted to result from the meteoric ablation of Si [Plane *et al.*, 2016]. Figure 7a illustrates the diurnal variation of the simulated OPO layer with full phosphorus chemistry (R1 - R38 in Table 1) at a mid-latitude site (54°N 12°E). This shows that the layer at 90 km exhibits a minimum around 0200 UT, which increases by ~90% to a maximum around 1400 UT (1448 LT). This is mostly caused by the photolysis of HOPO (in particular) and HPO₂, which prevent the formation of the more photolytically stable H₃PO₃ and H₃PO₄ (Table 1). Figure 7b illustrates the zonally-averaged annual mean OPO layer as a function of latitude and month. This shows that there is modest latitudinal variation, with a 32% increase from the minimum at northern high latitudes to a maximum between 30°S and 20°N. What is striking is the clear preponderance of OPO in the Southern Hemisphere: the latitude range where the layer peak concentration is greater than 50 cm⁻³ extends to 80°S, but only to 45°N.

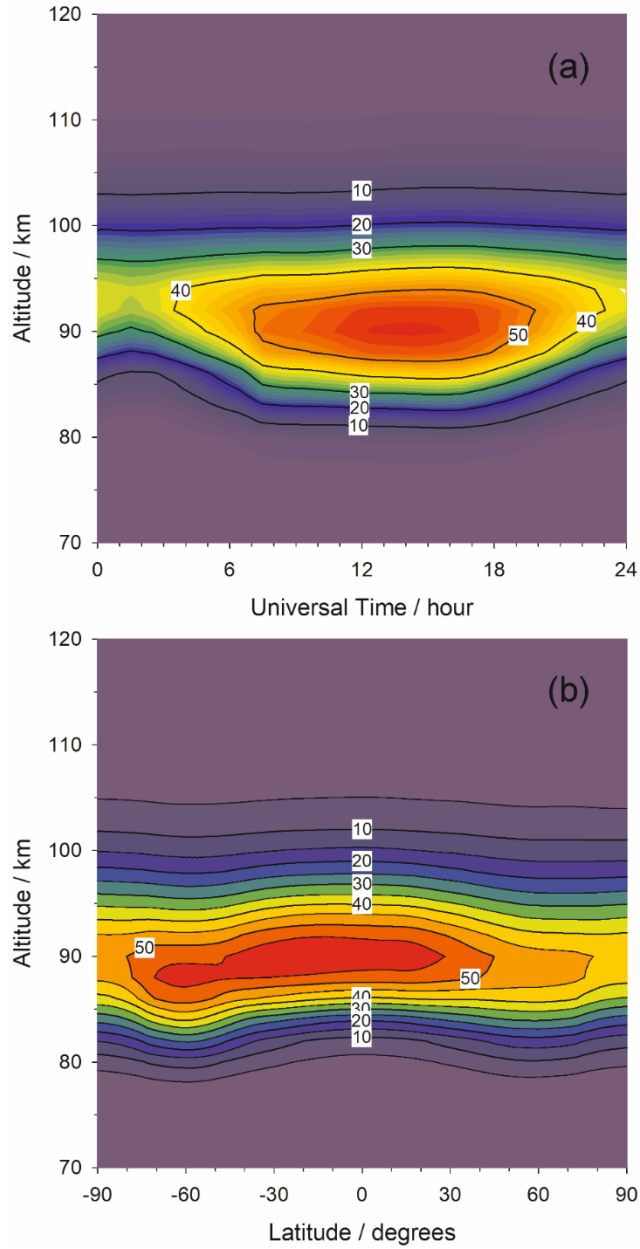


Figure 7. (a) Diurnal variation of OPO density (molecule cm^{-3}) as a function of altitude at the location 54°N 12°E , computed from hourly model output. (b) Zonally-averaged OPO density as a function of latitude and height, computed from monthly mean (diurnally-averaged) output. The data is averaged over 11

years (2004 - 2014).

This hemispheric difference is explained in Figure 8a, which shows the OPO vertical column density (VCD, integrated from 64 to 130 km) versus latitude and month. The complex variation, which when averaged over the year produces the greater amount of OPO at mid-to-high southern latitudes, arises from several factors. First, the seasonal variation of the PO MIF causes the vernal minima in OPO at mid-latitudes, and the autumnal maxima which extend to high latitudes in both hemispheres. Second, the minima that occur around the winter solstice at high latitudes ($>65^\circ$) are caused by the absence of photochemistry during the polar night, which reduces the recycling of HOPO and HPO_2 to OPO. The mid-summer minima at high latitudes are caused by two further factors. In the upper mesosphere there is a pronounced meridional circulation towards the winter pole [*Plane et al.*, 2015], where convergence of the products of meteoric ablation occurs (as seen in enhanced layers of Fe and Na [*Gardner et al.*, 2005]). The upwelling air at the summer pole causes divergence in the MLT, reducing the density of meteoric materials. Furthermore, the resulting colder temperatures favour the recombination reactions of OPO with H and OH (R6a, R6b and R8) which have negative temperature dependences (Table 1).

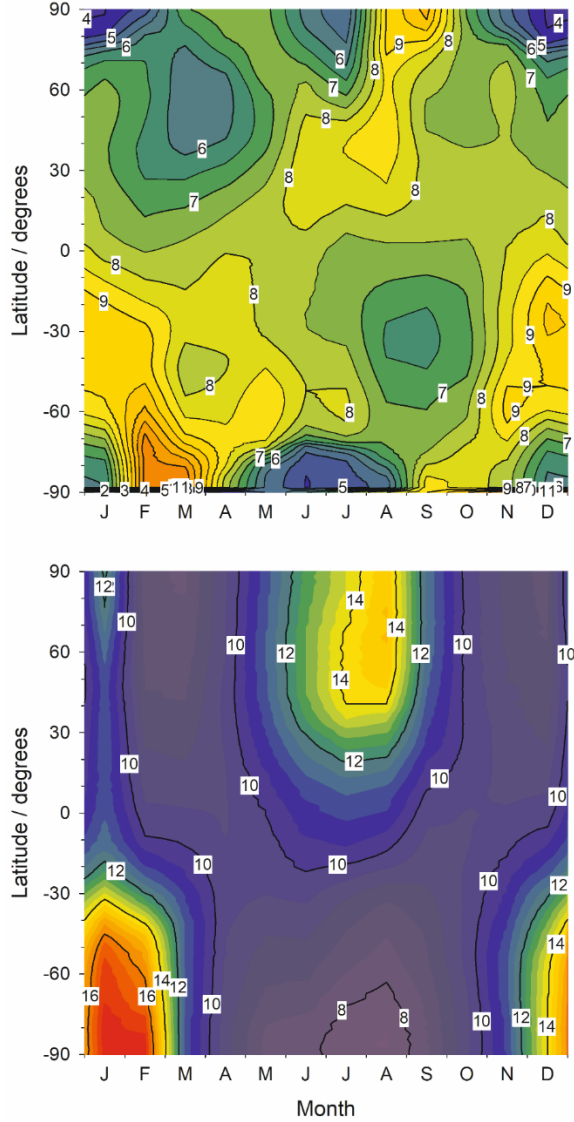


Figure 8. (a) Vertical column density (10^7 molecule cm^{-2}) of OPO as a function of latitude and season. (b) Percentage of phosphite in the vertical column of meteoric smoke particles, as a function of latitude and season. The data is averaged over 11 years (2004 - 2014).

OPO appears to be the only significant P-containing species which could potentially be observed spectroscopically, using the B-X transition band between 284 and 325 nm [Lei *et al.*, 2001; Douglas *et al.*, 2020]. The peak absorption cross section of this band is 5.7×10^{-17} cm^2 molecule $^{-1}$, calculated using the TD-DFT

method with the 6-311+g(2d,p) basis set [Bauernschmitt and Ahlrichs, 1996]. For a satellite stellar or solar occultation measurement with a typical optical path through the MLT of 300 km and peak OPO concentration of 50 cm^{-3} , the optical density would be 8.4×10^{-9} . Unfortunately, this is more than 2 orders of magnitude too small to be measured with current satellite-borne spectrometers such as the GOMOS instrument on ENVISAT [Fussen *et al.*, 2010] or the SOFIE instrument on AIM [Hervig *et al.*, 2017].

Figure 8b shows the percentage of ablated phosphorus in the form of phosphite, as a function of latitude and month. The percentage is calculated from the VCDs of MSP-PO_3 and MSP-PO_4 . The global annual average fraction of phosphite is 10.6%. However, the phosphite percentage is approximately twice as large during summer at mid- to high latitudes ($>50^\circ$). Although the colder temperatures during summer would favour formation of HOPO (R6b) over HPO_2 (R6a) (see the temperatures dependences in Table 1), once HPO_2 forms it is more likely to go on to form H_3PO_3 . This is because reaction with H back to OPO (R4) has a significant activation energy, and is much slower in the very cold summer upper mesosphere at high latitudes, where the typical summer-time temperature is $\sim 140 \text{ K}$ compared with a wintertime temperature of $\sim 220 \text{ K}$ [Plane *et al.*, 2015]: k_{14} becomes 56 times slower. Furthermore, the H_2O concentration is ~ 7 times larger as upwelling air over the summer pole brings fresh H_2O from the lower mesosphere, whereas the H atom concentration only increases by a factor of 2. This makes recombination of HPO_2 with H_2O (R7) more competitive with R14.

MSPs are too small to sediment rapidly compared to being transported by the residual circulation in the middle atmosphere into the lower stratosphere, principally inside the winter polar vortex [Bardeen *et al.*, 2008]. They then enter the troposphere principally along mid-latitude storm tracks, before mostly being deposited in broad bands between 40 and 60° N and 30 and 70° S [Brooke *et al.*, 2017]. Figure 9 is a world map showing the predicted deposition flux of phosphorus in MSPs. The flux is calculated from the MSP mass deposition rates reported by Brooke *et al.* [2017], scaled by a factor of 2.1×10^{-3} which is the ratio of the ablated mass flux of P [Carrillo-Sánchez *et al.*, 2020a] to the total ablated mass flux which becomes essentially FeMgSiO_4 particles [Carrillo-Sánchez *et al.*, 2020b] (note that this ratio uses the actual P flux, rather than the flux divided by 5 for the WACCM simulations in the MLT – Section 3.2). The highest P deposition rates of around $5 \times 10^{-8} \text{ g m}^{-2} \text{ yr}^{-1}$ are over the northern Rockies, Himalayas and southern Andes, compared with a global mean P deposition flux of $1 \times 10^{-8} \text{ g m}^{-2} \text{ s}^{-1}$. The estimated phosphite deposition flux from WACCM-P is then $1 \times 10^{-9} \text{ g m}^{-2} \text{ yr}^{-1}$, with a maximum of $5 \times 10^{-9} \text{ g m}^{-2} \text{ yr}^{-1}$. This global mean flux is close to the geometric mean of the recent estimate of phosphite production from lightning strikes of between 100–10,000 kg annually [Hess *et al.*, 2021]. Moreover, the phosphate within MSPs, which are mostly less than 100 nm in radius [Bardeen *et al.*, 2008; Brooke *et al.*, 2017], will be even more prone to lightning-initiated reduction, or aqueous phase chemistry during their residence in the highly acidic Junge layer [Saunders *et al.*, 2012],

than the phosphate buried within much larger meteorites.

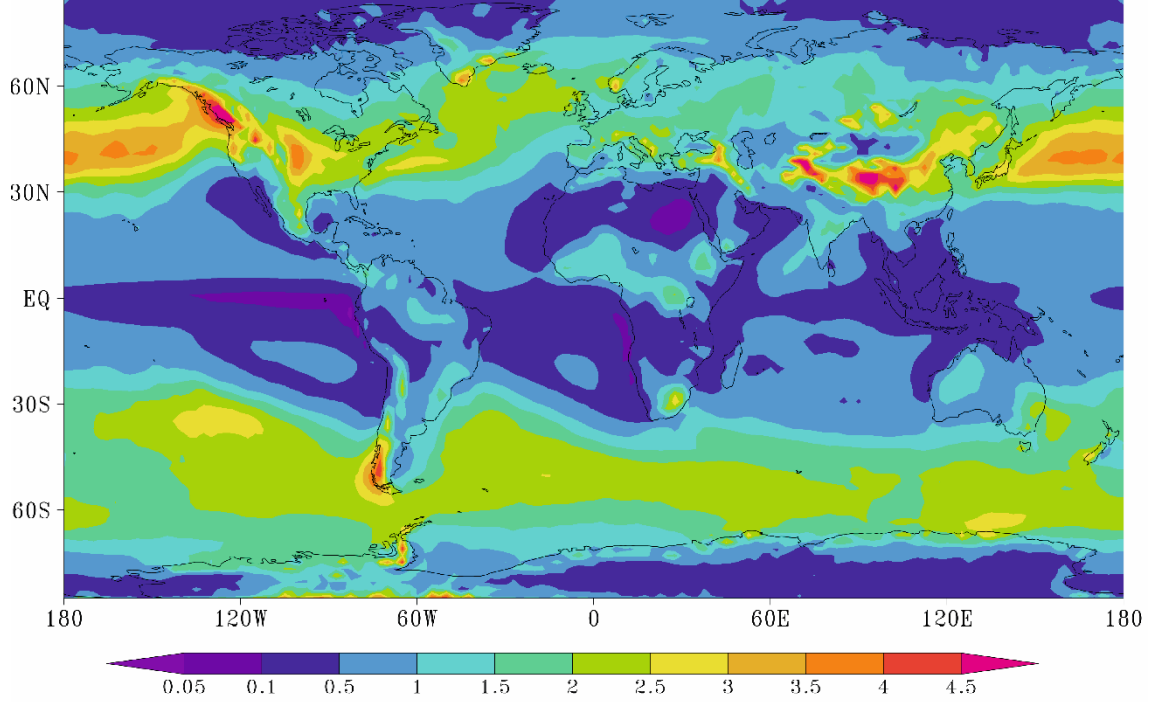


Figure 9. Map of the meteor-ablated phosphorus deposition flux ($10^{-8} \text{ g m}^{-2} \text{ yr}^{-1}$) from a 9-year run of the WACCM-CARMA model (December 2005 to November 2014). See *Brooke et al.* [2017] for further details.

5. Conclusions

In the present study we have developed a phosphorus chemistry network to explore possible routes from PO, OPO and P which ablate in the MLT from interplanetary dust particles entering the Earth’s atmosphere, to the stable reservoirs H_3PO_3 and H_3PO_4 which then become incorporated into meteoric smoke particles as metal phosphites and phosphates, respectively. While the network is partly constructed from reactions whose kinetics have been measured experimentally, many of the critical reactions have been (necessarily) assigned theoretical rate coefficients, estimated using a combination of electronic structure theory calculations and an established RRKM master equation treatment. The estimated fraction of 11% of ablated phosphorus forming metal phosphites is of course sensitive to these estimated rate coefficients. In particular, the branching ratio to formation of HPO_2 or HOPO in the recombination of H with OPO (R6a and R6b); the recombination of H_2O with HPO_2 to form H_3PO_3 (R7); the OH reactions forming HOPO_2 from OPO and HOPO (R8 and R9); and recombination of H_2O with HOPO_2 to form H_3PO_4 (R11).

Nevertheless, two important conclusions can be drawn. First, the ablation of phosphorus from interplanetary dust particles provides a substantial and continuous source of oxidized P to the surface in the form of sub-micron sized smoke particles. Second, a not insignificant fraction of the phosphorus is likely to be in the form of bio-available phosphites rather than phosphates, because of the unusual chemical conditions in the MLT with very large concentrations of O and H compared to OH. It will be interesting to explore in future work with WACCM-P how this fraction might have changed before and during the Great Oxygenation Event in the Paleoproterozoic era, approximately 2 Gyr ago [Lyons *et al.*, 2014].

Acknowledgements.

This study was supported by funding from the UK Science and Technology Facilities Council (grant ST/P000517/1). The model output data used in the paper is available at <https://doi.org/10.5281/zenodo.5146167>, and the electronic structure theory data is tabulated in the SI.

References

- Anicich, V. G. (2003), *An index of the literature for bimolecular gas phase cation-molecule reaction kinetics*, JPL Publication 03-19, Jet Propulsion Laboratory/California Institute of Technology, Pasadena, CA.
- Asplund, M., N. Grevesse, A. J. Sauval, and P. Scott (2009), The Chemical Composition of the Sun, in *Ann. Rev. Astron. Astrophys.*, edited by R. Blandford, J. Kormendy and E. van Dishoeck, pp. 481-522, Annual Reviews, Palo Alto, doi:10.1146/annurev.astro.46.060407.145222.
- Bardeen, C. G., O. B. Toon, E. J. Jensen, D. R. Marsh, and V. L. Harvey (2008), Numerical simulations of the three-dimensional distribution of meteoric dust in the mesosphere and upper stratosphere, *J. Geophys. Res.-Atmos.*, 113, art. no. D17202.
- Bauernschmitt, R., and R. Ahlrichs (1996), Treatment of electronic excitations within the adiabatic approximation of time dependent density functional theory, *Chem. Phys. Lett.*, 256, 454-464.
- Benna, M., P. R. Mahaffy, J. M. Grebowsky, J. M. C. Plane, R. V. Yelle, and B. M. Jakosky (2015), Metallic ions in the upper atmosphere of Mars from the passage of comet C/2013 A1 (Siding Spring), *Geophys. Res. Lett.*, 42, 4670-4675.
- Brooke, J. S. A., W. H. Feng, J. D. Carrillo-Sanchez, G. W. Mann, A. D. James, C. G. Bardeen, L. Marshall, D. S. S., and J. M. C. Plane (2017), Meteoric Smoke Deposition in the Polar Regions: A Comparison of Measurements With Global Atmospheric Models, *J. Geophys.-Atmos.*, 122, 11112-11130.
- Carrillo-Sánchez, J. D., D. L. Bones, K. M. Douglas, G. J. Flynn, S. Wirick, B. Fegley, T. Araki, B. Kaulich, and J. M. C. Plane (2020a), Injection of meteoric phosphorus into planetary atmospheres, *Planet. Space Sci.*, 187, art. no. 104926.
- Carrillo-Sánchez, J. D., J. C. Gómez-Martín, D. L. Bones, D. Nesvorný, P. Pokorný, M. Benna, G. J. Flynn, and J. M. C. Plane (2020b), Cosmic dust fluxes in the atmospheres of Earth, Mars, and Venus, *Icarus*, 335, art. no.: 113395.
- Carrillo-Sánchez, J. D., D. Nesvorný, P. Pokorný, D. Janches, and J. M. C. Plane (2016), Sources of cosmic dust in the Earth's atmosphere, *Geophys. Res. Lett.*, 43, 979-911, 986.
- Daly, S. M.,

Feng, W., Mangan, T. P., Gerding, M., & Plane, J. M. C. (2020), The Meteoric Ni Layer in the Upper Atmosphere, *J. Geophys. Res. - Space Phys.*, *125*, art. no.: e2020JA028083. Danabasoglu, G., J.-F. Lamarque, J. Bacmeister, D. A. Bailey, A. K. DuVivier, J. Edwards, L. K. Emmons, J. Fasullo, R. R. Garcia, A. Gettelman, et al. (2020), The Community Earth System Model version 2 (CESM2), *J. Adv. Mod. Earth Sys.*, *12*, art. no.: e2019MS001916. Douglas, K. M., M. A. Blitz, T. P. Mangan, and J. M. C. Plane (2019), Experimental Study of the Removal of Ground- and Excited-State Phosphorus Atoms by Atmospherically Relevant Species, *J. Phys. Chem. A*, *123*, 9469-9478. Douglas, K. M., M. A. Blitz, T. P. Mangan, C. M. Western, and J. M. C. Plane (2020), Kinetic Study of the Reactions $\text{PO} + \text{O}_2$ and $\text{PO}_2 + \text{O}_3$ and Spectroscopy of the PO Radical, *J. Phys. Chem. A*, *124*, 7911-7926. Feng, W., D. R. Marsh, M. P. Chipperfield, D. Janches, J. Höffner, F. Yi, and J. M. C. Plane (2013), A global atmospheric model of meteoric iron, *J. Geophys. Res.-Atmos.*, *118*, 9456-9474. Florescu-Mitchell, A. I., and J. B. A. Mitchell (2006), Dissociative recombination, *Phys. Rep. Rev. Phys. Lett.*, *430*, 277-374. Frisch, M. J., G. W. Trucks, H. B. Schlegel, G. E. Scuseria, M. A. Robb, J. R. Cheeseman, G. Scalmani, V. Barone, G. A. Petersson, H. Nakatsuji, et al. (2016), Gaussian 16 Rev. B.01, edited, Wallingford, CT. Fussen, D., F. Vanhellemont, C. Tetard, N. Mateshvili, E. Dekemper, N. Loodts, C. Bingen, E. Kyrola, J. Tamminen, V. Sofieva, et al. (2010), A global climatology of the mesospheric sodium layer from GOMOS data during the 2002-2008 period, *Atmos. Chem. Phys.*, *10*, 9225-9236. Gardner, C. S., A. Z. Liu, and Y. Guo (2017), Vertical and horizontal transport of mesospheric Na: Implications for the mass influx of cosmic dust, *J. Atmos. Sol. Terr. Phys.*, *162*, 192-202. Gardner, C. S., J. M. C. Plane, W. Pan, T. Vondrak, B. J. Murray, and X. Chu (2005), Seasonal variations of the Na and Fe layers at the South Pole and their implications for the chemistry and general circulation of the polar mesosphere, *J. Geophys. Res.-Atmos.*, *110*, art. no. D1030210. Georgievskii, Y., and S. J. Klippenstein (2005), Long-Range Transition State Theory, *J. Chem. Phys.*, *122*, art. no.: 194103. Gettelman, A., M. J. Mills, D. E. Kinnison, R. R. Garcia, A. K. Smith, D. R. Marsh, S. Tilmes, F. Vitt, C. G. Bardeen, J. McInerney, et al. (2019), The Whole Atmosphere Community Climate Model Version 6 (WACCM6), *124*, 12380-12403. Gibard, C., I. B. Gorrell, E. I. Jimenez, T. P. Kee, M. A. Pasek, and R. Krishnamurthy (2019), Geochemical Sources and Availability of Amidophosphates on the Early Earth, *Angew. Chem.-Int. Edit.*, *58*, 8151-8155. Gilbert, R. G., and S. C. Smith (1990), *Theory of Unimolecular and Recombination Reactions*, Blackwell, Oxford. Glowacki, D. R., C. H. Liang, C. Morley, M. J. Pilling, and S. H. Robertson (2012), MESMER: An Open-Source Master Equation Solver for Multi-Energy Well Reactions, *Journal of Physical Chemistry A*, *116*, 9545-9560. Grebowsky, J. M., and A. C. Aikin (2002), In Situ Measurements of Meteoric Ions, in *Meteors in the earth's atmosphere*, edited by E. Murad and I. P. Williams, pp. 189-214, Cambridge University Press, Cambridge. Hervig, M. E., J. S. A. Brooke, W. Feng, C. G. Bardeen, and J. M. C. Plane (2017), Constraints on Meteoric Smoke Composition and Meteoric Influx Using SOFIE Observations With Models, *J. Geophys. Res.-Atmos.*, *122*, 13,495-413,505. Hess,

B. L., S. Piazzolo, and J. Harvey (2021), Lightning strikes as a major facilitator of prebiotic phosphorus reduction on early Earth, *Nat. Comm.*, *12*, art. no. 1535.

Kopp, E., P. Eberhardt, U. Herrmann, and L. G. Björn (1985), Positive ion composition of the high-latitude summer D region with noctilucent clouds, *J. Geophys. Res.-Atmos.*, *90*, 13041-13053.

Langowski, M. P., C. von Savigny, J. P. Burrows, W. Feng, J. M. C. Plane, D. R. Marsh, D. Janches, M. Sinnhuber, A. C. Aikin, and P. Liebing (2015), Global investigation of the Mg atom and ion layers using SCIAMACHY/Envisat observations between 70 and 150 km altitude and WACCM-Mg model results, *Atmos. Chem. Phys.*, *15*, 273-295.

Lei, J., A. Teslja, B. Nizamov, and P. J. Dagdigan (2001), Free-jet electronic spectroscopy of the PO₂ radical, *J. Phys. Chem. A*, *105*, 7828-7833.

Lyons, T. W., C. T. Reinhard, and N. J. Planavsky (2014), The rise of oxygen in Earth's early ocean and atmosphere, *Nature*, *506*, 307-315.

Maciá, E. (2005), The role of phosphorus in chemical evolution, *Chem. Soc. Rev.*, *34*, 691-701.

Marsh, D. R., D. Janches, W. Feng, and J. M. C. Plane (2013), A global model of meteoric sodium, *J. Geophys. Res.-Atmos.*, *118*, 11,442-411,452.

Montgomery, J. A., Jr., M. J. Frisch, J. W. Ochterski, and G. A. Petersson (1999), A complete basis set model chemistry. VI. Use of density functional geometries and frequencies, *J. Chem. Phys.*, *110*, 2822-2827.

Nesvorný, D., D. Janches, D. Vokrouhlický, P. Pokorný, W. F. Bottke, and P. Jenniskens (2011), Dynamical Model for the Zodiacal Cloud and Sporadic Meteors, *Astrophys. J.*, *743*, 129.

Pasek, M. A. (2008), Rethinking early Earth phosphorus geochemistry, *Proceedings of the National Academy of Sciences*, *105*, 853-858.

Plane, J. M. C., W. Feng, and E. C. M. Dawkins (2015), The mesosphere and metals: chemistry and changes, *Chem. Rev.*, DOI: 10.1021/cr500501m.

Plane, J. M. C., W. Feng, J. C. Gómez Martín, M. Gerding, and S. Raizada (2018), A new model of meteoric calcium in the mesosphere and lower thermosphere, *Atmos. Chem. Phys.*, *18*, 14799-14811.

Plane, J. M. C., J. C. Gomez-Martin, W. H. Feng, and D. Janches (2016), Silicon chemistry in the mesosphere and lower thermosphere, *J. Geophys. Res.-Atmos.*, *121*, 3718-3728.

Redfield, A. C. (1958), The biological control of chemical factors in the environment, *Am. Scientist*, *46*, 205-221.

Reinhard, C. T., N. J. Planavsky, B. C. Gill, K. Ozaki, L. J. Robbins, T. W. Lyons, W. W. Fischer, C. Wang, D. B. Cole, and K. O. Konhauser (2017), Evolution of the global phosphorus cycle, *Nature*, *541*, 386-389.

Saunders, R. W., S. Dhomse, W. S. Tian, M. P. Chipperfield, and J. M. C. Plane (2012), Interactions of meteoric smoke particles with sulphuric acid in the Earth's stratosphere, *Atmos. Chem. Phys.*, *12*, 4387-4398.

Tobiska, W. K., T. Woods, F. Eparvier, R. Viereck, L. Floyd, D. Bouwer, G. Rottman, and O. R. White (2000), The SOLAR2000 empirical solar irradiance model and forecast tool, *J. Atmos. Sol. Terr. Phys.*, *62*, 1233-1250.

Viehl, T. P., J. M. C. Plane, W. Feng, and J. Höffner (2016), The photolysis of FeOH and its effect on the bottomside of the mesospheric Fe layer, *Geophys. Res. Lett.*, *43*, 1373-1381.

Vondrak, T., J. M. C. Plane, S. Broadley, and D. Janches (2008), A chemical model of meteoric ablation, *Atmos. Chem. Phys.*, *8*, 7015-7031.

Figure Captions.

Figure 1. Schematic diagram of the neutral and ion-molecule chemistry of phosphorus in the earth’s mesosphere and lower thermosphere. Neutral and ionized P species are shown in green and blue boxes, respectively. The green arrows indicate the important pathway from OPO to H_3PO_3 ; the red arrows show the reactions forming H_3PO_4 ; and the blue arrows indicate reactions that have been studied experimentally.

Figure 2. Potential energy surfaces calculated at the CBS-QB3 level of the theory [Montgomery *et al.*, 1999]: (a) OPO + H forming HPO_2 or HOPO; (b) HPO_2 recombining with H_2O to form H_3PO_3 (phosphonic acid).

Figure 3. Potential energy surfaces calculated at the CBS-QB3 level of the theory [Montgomery *et al.*, 1999]: (a) HOPO + OH to form HOPO_2 (black route) or OPO + H_2O (red route); (b) HOPO_2 recombining with H_2O to form H_3PO_4 (phosphoric acid).

Figure 4. Absorption cross sections of H_3PO_3 , H_3PO_4 , HOPO_2 , HPO_2 and HOPO computed at the TD//B3LYP/6-311+g(2d,p) level of theory [Frisch *et al.*, 2016]. The vertical arrows indicate upper limits to the photolysis thresholds, computed from the relevant bond dissociation energies at the CBS-QB3 level of theory [Montgomery *et al.*, 1999].

Figure 5. Global annual mean injection rates of PO (representing P + PO + OPO) and Fe from meteoric ablation. The injection profiles predicted by the CABMOD-ZoDY model [Carrillo-Sánchez *et al.*, 2020a; Carrillo-Sánchez *et al.*, 2020b] have been divided by a factor of 5.0 for input into the WACCM6 model (see text).

Figure 6. Mean vertical profiles of P-containing species averaged over 11 years (2004 -2014) at mid-latitudes (54°N) : (a) Photolysis of P species (R34 - R38) turned off and MSP-forming condensation reactions (R30 - R33) turned off; (b) Photolysis (R34 - R38) turned on, MSP formation (R30 - R33) turned off; (c) Photolysis and MSP formation turned on (i.e. full P chemistry R1 – R38 turned on).

Figure 7. (a) Diurnal variation of OPO density (molecule cm^{-3}) as a function of altitude at the location 54°N 12°E, computed from hourly model output. (b) Zonally-averaged OPO density as a function of latitude and height, computed from monthly mean (diurnally-averaged) output. The data is averaged over 11 years (2004 - 2014).

Figure 8. (a) Vertical column density (10^7 molecule cm^{-2}) of OPO as a function of latitude and season. (b) Percentage of phosphite in the vertical column of meteoric smoke particles, as a function of latitude and season. The data is averaged over 11 years (2004 - 2014).

Figure 9. Map of the meteor-ablated phosphorus deposition flux (10^{-8} g m^{-2} yr^{-1}) from a 9-year run of the WACCM-CARMA model (December 2005 to November 2014). See Brooke *et al.* [2017] for further details.

Tables

Table 1. Phosphorus chemistry in the MLT.